The Photometry of Undersampled Point Spread Functions

Tod R. Lauer

National Optical Astronomy Observatories[1], P. O. Box 26732, Tucson, AZ 85726

Electronic mail: lauer@noao.edu

ABSTRACT

An undersampled point spread function may interact with the microstructure of a solid-state detector such that the total flux detected can depend sensitively on where the PSF center falls within a pixel. Such *intra-pixel* sensitivity variations will not be corrected by flat field calibration and may limit the accuracy of stellar photometry conducted with undersampled images, as are typical for *Hubble Space Telescope* observations. The total flux in a stellar image can vary by up to 0.03 mag in F555W WFC images depending on how it is sampled, for example. For NIC3, these variations are especially strong, up to 0.39 mag, strongly limiting its use for stellar photometry. Intra-pixel sensitivity variations can be corrected for, however, by constructing a well-sampled PSF from a dithered data set. The reconstructed PSF is the convolution of the optical PSF with the pixel response. It can be evaluated at any desired fractional pixel location to generate a table of photometric corrections as a function of relative PSF centroid. A caveat is that the centroid of an undersampled PSF can also be affected by the pixel response function, thus sophisticated centroiding methods, such as cross-correlating the observed PSF with its fully-sampled counterpart, are required to derive the proper photometric correction.

Subject headings: techniques:image processing — techniques:photometric

1. Introduction

The study of stellar populations has been revolutionized by the techniques of crowded-field photometry applied to *Hubble Space Telescope* images. Ironically, however, nearly all *HST* images are undersampled and are thus not optimal for such problems. The information missing from undersampled images makes it difficult to detect faint sources, eliminate cosmic ray hits, register

---

[1]The National Optical Astronomy Observatories are operated by the Association of Universities for Research in Astronomy, Inc., under cooperative agreement with the National Science Foundation.

different exposures, accurately represent the stellar point spread function (PSF), and so on. These problems are well known to practitioners of crowded-field photometry, and can be partially countered by using impressive software packages such as ALLFRAME (Stetson 1994), DoPHOT (Schechter, Mateo, & Saha 1993), or CCDCAP (Mighell 1997), which are specially tuned to extract information from multi-image data sets that may be poorly represented in any single image. The effects of undersampling on the detected flux of a stellar image, itself, may be less apparent, but are potentially important. While one might assume that a photon will generate an electron that will land in one pixel or another, regardless of how the sampling is done, in reality the complex microstructure of a CCD or any other solid-state detector may cause its response to vary significantly over the area of a single pixel. In this paper I present a method to calibrate and correct such *intra-pixel* sensitivity variations, with particular application to *HST* WFPC2 and NIC3 images.

In a well-sampled image the pixel spacing or sampling frequency is sufficient to completely characterize its structural content on all spatial scales; in a poorly sampled image fine-scale structure may be present that can interact with the yet higher spatial frequencies associated with the detector microstructure. Jorden, Deltron, & Oates (1994) used a pinhole projector to measure the intra-pixel response of a variety of CCDs. Their experiments showed that the total detected flux of an undersampled PSF can vary strongly ($> \pm 10\%$) with centering within a pixel, source color, and differences among the gate structure of the various CCDs. Front-illuminated devices showed the strongest effects, but significant variations could still be seen with rear-illuminated CCDs. Not surprisingly, the response varied differently as a function of the row versus column position, given the anisotropic structure of CCDs.

Real astronomical cameras are difficult to calibrate with such laboratory experiments, given the sensitivity to the degree of PSF undersampling, but intra-pixel effects may be detected through a "dithered" set of images of a star field, that is images slightly offset from each other by a fraction of a pixel. Holtzman et al. (1995) used such images of the ω Cen globular cluster to show that the detected stellar flux varied by a few percent as a function of fractional column position in the WFPC-2 CCDs. While such a small effect may of little concern for most WFPC-2 programs, the situation is far different in NIC3 images. Here the strong undersampling, coupled with the particular microstructure of the NICMOS arrays (which are not CCDs) causes the detected flux in a stellar image to vary by up to ± 0.2 mag in the bluest (and hence most poorly sampled) colors. Clearly, this strongly limits use of NIC3 for stellar photometry work.

Calibration of the camera response to undersampled images can be done in a variety of ways, given a dithered image set of point sources. My approach is to reconstruct a fully sampled "superimage" from the data set, which can be then used to make "observed" images true to the original sampling, but with any desired spatial offset; one can then simply measure how the integrated flux of a point source varies with its fractional offset with respect to the pixel grid. Any single image can be expressed as

$$I(x,y) = O(x,y) * P(x,y) \left(\mathrm{III}(x,y) * \mathcal{R}(x,y) \right), \tag{1}$$

where O is the intrinsic projected appearance of the astronomical field being imaged, P is the PSF due to the telescope and camera optics, $\mathrm{III}(x, y)$ is a two-dimensional array of sampling points

$$\mathrm{III}(\mathrm{ax}, \mathrm{ay}) \equiv \frac{1}{|\mathrm{a}|^2} \sum_{\mathrm{i}=-\infty}^{+\infty} \sum_{\mathrm{j}=-\infty}^{+\infty} \delta\left(\mathrm{x} - \frac{\mathrm{i}}{\mathrm{a}}\right) \delta\left(\mathrm{y} - \frac{\mathrm{j}}{\mathrm{a}}\right), \tag{2}$$

and $*$ means convolution. The critical term for the present discussion is $\mathcal{R}(x, y)$, the generally unknown spatial response of the pixel, itself. This term not only includes the sensitivity response as a function location within the pixel, but also any diffusion of photons or photoelectrons within the device — its extent may thus be larger than that of a single pixel.

Producing a dithered image set by stepping the detector a fractional amount in x and y can be used to produce a more finely sampled superimage. When the dithers are done in a regular $N \times N$ pattern of subpixel steps (of relative size $1/N$),

$$\begin{aligned} I_S(x, y) &= O(x, y) * P(x, y) \sum_{i=0}^{N-1} \sum_{j=0}^{N-1} \mathrm{III}\left(\mathrm{x} - \frac{\mathrm{i}}{\mathrm{N}}, \mathrm{y} - \frac{\mathrm{j}}{\mathrm{N}}\right) * \mathcal{R}(\mathrm{x}, \mathrm{y}), \\ &= (O(x, y) * P(x, y) * \mathcal{R}(x, y))\, \mathrm{III}(\mathrm{Nx}, \mathrm{Ny}). \end{aligned} \tag{3}$$

The new superimage thus has an effective PSF

$$P'(x, y) = P(x, y) * \mathcal{R}(x, y). \tag{4}$$

For severely undersampled images, $\mathcal{R}$ may actually be more important than the core structure of P for setting the effective resolution of P'. If N is large enough such that P' is fully sampled ($N = 3$ for WFPC-2 is sufficient), then P' can be interpolated to any desired location with respect to the original undersampled pixel array. Drawing every Nth pixel in x and y from the superimage generates an image as would have been observed at the given position. Comparing the integrated flux in the interpolated-undersampled PSF to that in P' thus allows the photometric effects of undersampling to be measured for any desired fractional location with respect to the original grid. Note that $\mathcal{R}$ need not be determined itself, since it is implicitly included in P', and its effects depend critically on the structural content of P in any case.

The tricky step is generating a fully-sampled superimage. While it may be possible to step the detector position in a regular subpixel sampling grid, in practice this may be difficult. Sub-pixel dithers have been used in many WFPC-2 programs, for example, but were often not executed with enough precision to fall on a regular pattern. In this case, the simple interlacing of the dithered image set implied by equation (3) cannot be done. Reconstruction of a well-sampled superimage from a set of undersampled images is a difficult problem if the geometric relationships among the images are complex. For the simple case, however, where the images in the set are related by purely translational (if arbitrary) offsets, the sampling grid is spatially constant, and the intrinsic object, PSF, and detector properties do not vary over the set, it is possible to construct a superimage in closed form through a complex linear combination of the images in

Fourier space (Lauer 1999). While these requirements may sound highly and perhaps impossibly idealized, in practice they can be realized in *HST* observations with both WFPC2 and NICMOS, for example, if the dither offsets are relatively small with respect to any changes in the angular pixel sampling frequency, and the observations are obtained over a short enough time span such that any focus changes, source variability, and so on, are unimportant. In passing, I note that the *Drizzle* algorithm (Fruchter & Hook 1999) has proven to be an extremely popular and versatile tool for building superimages from *HST* data sets; however, *Drizzle* does not guarantee that the superimage is well-sampled, and since it also introduces a variable blurring function on the finest scales, I am concerned that it may not be suited to the present application.

2. Calibrating the Photometry of an Undersampled PSF

2.1. Construction of a Well-Sampled PSF

In greater detail, the method of PSF reconstruction advocated here involves stacking the set of dithered images in the Fourier domain. The Fourier transform of a discretely sampled data set is periodic, repeating to $\pm\infty$ in both x and y. When an image is undersampled, or aliased, the higher order "satellites" in the Fourier domain overlap with and contaminate the fundamental transform. This contamination cannot be eliminated in any single image, but as the object being imaged is shifted with respect to the pixel grid, the phases within the Fourier satellites vary. With a sufficient number of dithered images, each having different phases, the aliasing can be eliminated algebraically. The sampling frequency in the final superimage is determined by the spatial scale at which P' no longer has significant power. This approach is nicely summarized by Bracewell (1978) for the case of one-dimensional data; I present a tutorial on its extension to images, with particular application to *HST* WFPC-2 images, in Lauer (1999). The attractive features of this method are that the superimage is well-sampled, there are no arbitrary parameters controlling its construction, and there is no blurring at the Nyquist scale. The method requires a minimum of N^2 images with non-degenerate dithers to construct a superimage with $N \times N$ subsampling; when more images are available the superimage is overdetermined and becomes the best-fit to the dither set.

The *HST* WFPC-2 and NICMOS imagers provide contrasting test cases for exploring the effects of intra-pixel sensitivity variations. Intra-pixel effects are subtle in the WFC chips of WFPC-2, but severe in the NIC3 camera. Figures 1 to 4 show PSFs reconstructed with 3×3 subsampling for the V (F555W) and I (F814W) filters in the WFC camera of WFPC-2, and the J (F110W) and H (F160W) filters for NIC3. The WFPC-2 PSFs were constructed from dithered observations of ω Cen (STScI program 4819) actually obtained by the WFPC-2 IDT for the purpose of understanding variations in the WFPC-2 PSF as a function of pixel location. The image set consists of 20 images in each of two filters, F555W, and F814W. The dither pattern consists of $0\rlap{.}''025$ steps in the row and column directions, the 20 images mapping out a $0\rlap{.}''075 \times 0\rlap{.}''1$
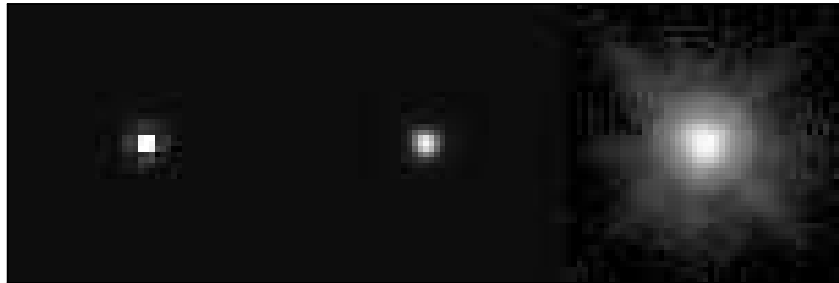
Fig. 1.— Reconstruction of an *HST* WFC PSF with 3×3 subsampling is shown based on 20 dithered F555W images of a star in ω Cen. The image at left shows a linear stretch of the PSF with the original sampling ($0\rlap{.}''10$ pixels). The central image shows the reconstructed PSF with the same intensity stretch with the full 3×3 subsampling. The last image is a logarithmic stretch (with dynamic range 3.5 in log units) of the reconstructed PSF. Each subimage is $1\rlap{.}''7 \times 1\rlap{.}''7$ in size.
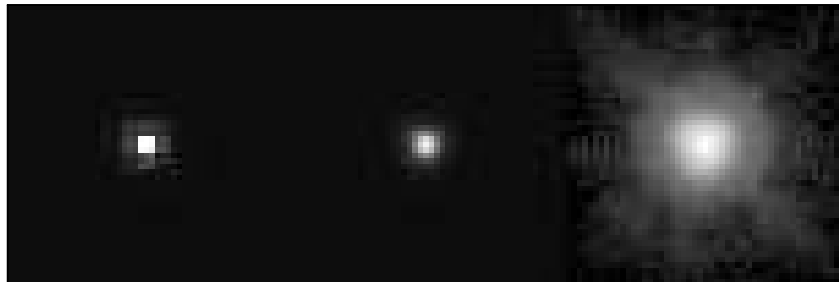
Fig. 2.— Reconstruction of an *HST* WFC PSF in the F814W filter, as in Figure 1. Both figures show the same star.
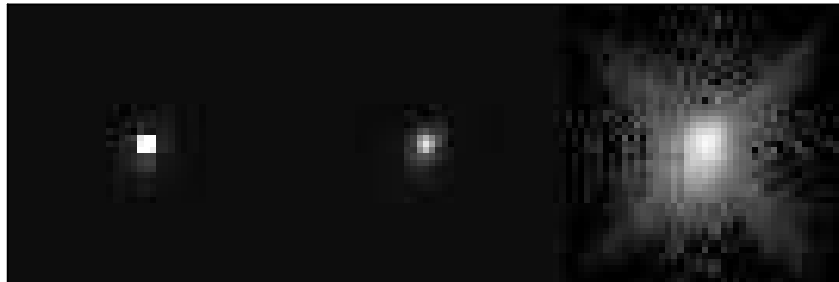
Fig. 3.— Reconstruction of an *HST* NIC3 F110W (J-band) PSF with 3×3 subsampling based on dithered images obtained as part of the *Hubble Deep Field South* program. The star shown is the brightest source in the NIC3 HDFS field. The image at left shows a linear stretch of the PSF with the original sampling ($0\rlap{.}''20$ pixels). The central image shows the reconstructed PSF with the same intensity stretch with the full 3×3 subsampling. The last image is a logarithmic stretch (with dynamic range 3.5 in log units) of the reconstructed PSF. Each subimage is $3\rlap{.}''0 \times 3\rlap{.}''0$ in size.
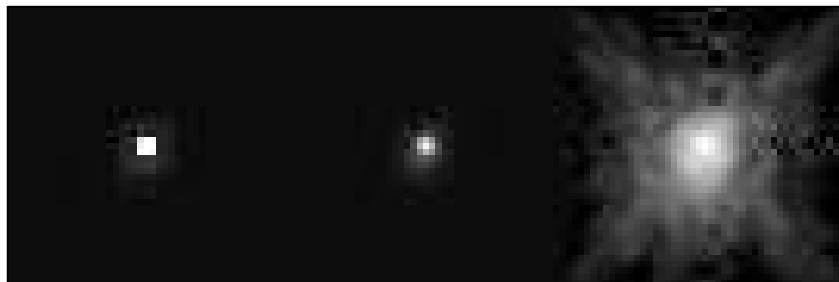
Fig. 4.— Reconstruction of an *HST* NIC3 PSF in the F160W (H-band) filter, as in Figure 3. Both figures show the same star.

rectangle with a square grid.

The NIC3 PSFs were constructed from images obtained for the *Hubble Deep Field South* program. The image set comprised 146 exposures, of which 98 were used (the star in the discarded images was either out of the field, or too close to its border). The PSFs shown are from the brightest star in the HDF-S field. The HDF-S dither pattern consisted both of small and large angular offsets, largely dictated by the needs of the other cameras used in the HDF-S program. While this data set was fine for the present purposes, in many ways the dither pattern was far from optimal, an issue that I will discuss in further detail below.

2.2. Mapping the Photometric Variation of an Undersampled PSF

It is simple to calibrate the effects of intra-pixel sensitivity variations and undersampling on a PSF, once P' has been constructed. Since P' is well-sampled, its centroid can be shifted to any desired fractional pixel location, without loss of resolution or information. Once shifted, coarse samples can be drawn from P' to simulate a PSF, $P_0(\delta x, \delta y)$, as would be observed at that location. P_0 is thus

$$P_0(\delta x, \delta y) = P'(x - \delta x, y - \delta y)\mathrm{III}(\mathrm{x}, \mathrm{y}), \tag{5}$$

where the III function refers to the spacing of the detector (rather than subsampled) pixels. The photometric error, $\epsilon(\delta x, \delta y)$, at the given offset is

$$\epsilon(\delta x, \delta y) = \int_{-\infty}^{+\infty} \int_{-\infty}^{+\infty} P_0(\delta x, \delta y) dx \ dy \bigg/ \int_{-\infty}^{+\infty} \int_{-\infty}^{+\infty} P'(x, y) dx \ dy \ - \ 1 \tag{6}$$

One can thus systematically map ϵ over the entire domain of fractional centroid offsets at any desired resolution; the map essentially consists of a lookup table of photometric offsets to be applied to a reduced photometric data set. It is critical to use a method of interpolation for P' that does not degrade the resolution; I do this with sinc-function interpolation, which is the theoretically appropriate sampling kernel for well-sampled data. Lastly, I emphasize that no "integration over a pixel" is included in equation (5), nor should be. Remember, P' already reflects convolution of the optical PSF with the detector pixel response, thus this integration has already implicitly taken place.

Figures 5 to 8 show the error maps for the WFPC-2 and NIC3 PSFs as   a function of the fractional pixel location of the PSF centroid. The square area of the maps corresponds to the domain $-1/2 < \delta x < 1/2$, $-1/2 < \delta y < 1/2$, in steps of 0.05 pixels; $(\delta x, \delta y) = (0, 0)$ is at the center of the maps. An important caveat is that in practice finite limits of integration must be used in equation (6), thus the absolute size of the errors will vary somewhat with aperture. In the present case I measure the flux in a $1''\!.5 \times 1''\!.5$ box for the WFC PSFs and a $3''\!.0 \times 3''\!.0$ box for NIC3. Overexposed stellar images show that significant scattered light falls outside these limits, but in the case of WFPC-2 at least, the aperture includes nearly all the pixels above the background for stellar images not saturated in the core.
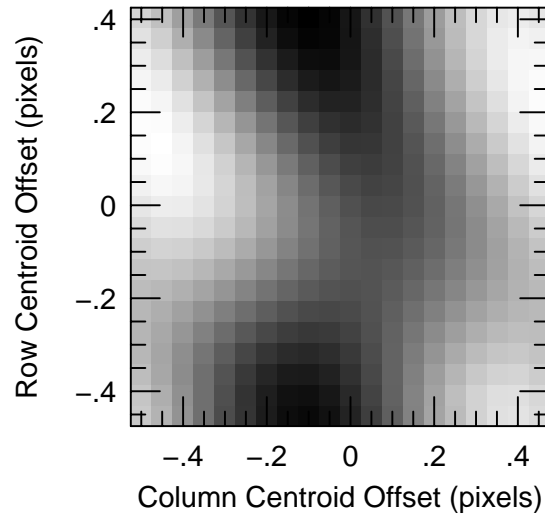
Fig. 5.— The photometric error caused by undersampling is shown for the V-band (F555W) WFC PSF (presented in Figure 1) as a function of fractional pixel location of the PSF centroid. The area shown is that of a single pixel, corresponding to centroid offsets of $-1/2 < \delta x < 1/2$, $-1/2 < \delta y < 1/2$, in units of the original WFC pixel; the position of no PSF offset, that is a PSF centered precisely on a WFC pixel is at the center of the map. Results are presented in steps of 0.05 pixels in x and y. The gray scale is linear with the stretch set to the full range of photometric error measured, with white corresponding to 0.016 mag of excess flux, and black to a 0.014 mag deficit. The maximal flux is actually detected at the x margins, corresponding to a PSF centered between columns on the WFC CCDs.
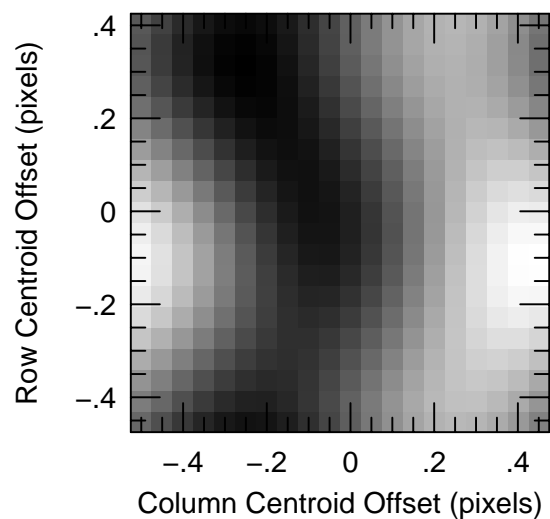
Fig. 6.— The photometric error caused by undersampling is shown for the I-band (F814W) WFC PSF (presented in Figure 2). The stretch now corresponds to 0.013 mag excess to 0.011 mag deficit.
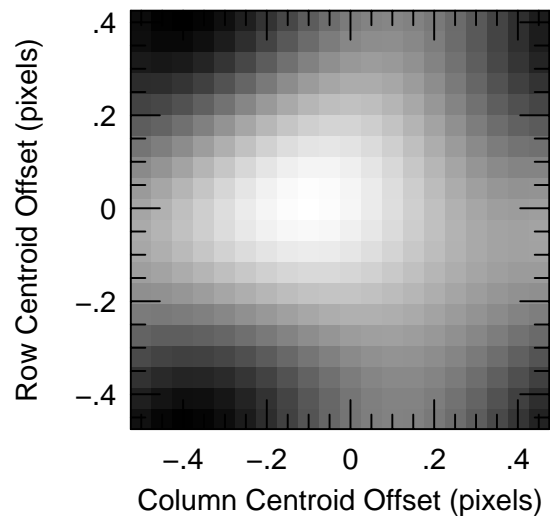

Fig. 7.— The photometric error caused by undersampling is shown for the J-band (F110W) NIC3 PSF (presented in Figure 3). The stretch now corresponds to 0.22 mag excess to 0.17 mag deficit.
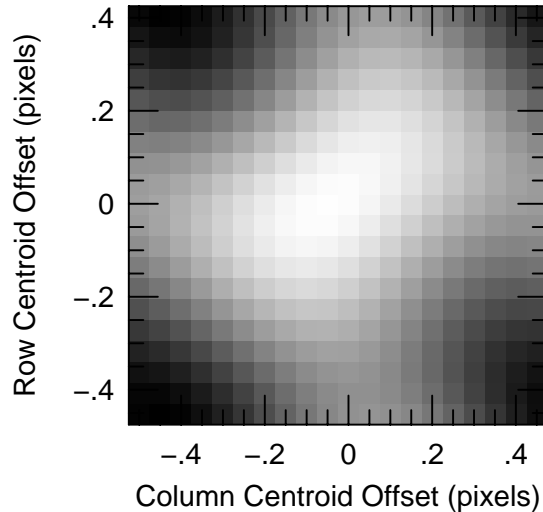
Fig. 8.— The photometric error caused by undersampling is shown for the H-band (F160W) NIC3 PSF (presented in Figure 4). The stretch now corresponds to 0.12 mag excess to 0.09 mag deficit.

The WFC error maps show that the photometric effects of undersampling are subtle, but are still significant for bright sources with sufficient signal. The error map for the WFC V-band PSF has a peak-to-peak range of 0.030 mag, and an rms dispersion of 0.008 mag. The effects of undersampling are slightly reduced in I-band, as might be expected given its larger PSF width; the peak-to-peak error range is 0.023 mag, with a 0.006 mag dispersion. The random color error is thus limited to 0.01 mag. Intriguingly, however, the V and I maps qualitatively resemble each other, thus errors in V and I may correlated depending on how the telescope was pointed for the two images. Both filters show that the error maps are anisotropic in the CCD row (y) and column (x), with maximal flux ($\epsilon > 0$) actually corresponding to when the PSF falls between two CCD columns; however, the error maps cannot be simply described as separable x and y functions. These results are in excellent agreement with the simple measurements presented in Holtzman et al. (1995), who found little dependence of the photometry on fractional row location, but a few percent variation dependent on fractional column location, again with more light detected for stars centered between columns. Note that this implies that the intra-pixel response itself for CCDs is more complex than a simple picture that might have fairly uniform pixels separated by less sensitive "cracks." Jorden, Deltron & Oates (1994) indeed emphasized that at some wavelengths the CCD column stops corresponded to regions of enhanced sensitivity. At the same time, they did see this pattern reverse in sign at other wavelengths — the reader is cautioned that the present results are valid only for the F555W and F814W filters.

If undersampling effects are subtle in the WFPC-2 CCDs, they completely dominate the photometric errors of stellar photometry done with the NIC3 camera. The peak-to-peak error

range in the NIC3 J-band is 0.39 mag; the dispersion is 0.10 mag. The H-band PSF is broader, given the longer wavelength of the bandpass, thus reducing the undersampling effects — still the errors remain large, with a 0.22 mag peak-to-peak range, and a 0.06 mag dispersion. The greatest sensitivity indeed occurs for PSFs centered on a pixel, unlike the case for the WFPC2 CCDs; given the architecture of the NICMOS arrays, the picture of loosing light in the cracks between the pixels may be more valid for these devices.

A critical issue is understanding if the present calibrations can be used to correct for undersampling effects in WFPC2 or NIC3 images. Unfortunately in the case of WFPC2, it appears that the form of the PSF core is the dominant contributor to undersampled structure. Maps made with different stars within the same image set have error maps that differ significantly from each other. The WFC PSFs shown above were taken from a bright star near the center of the W2 CCD of WFPC2. A map generated from another star only 147 pixels away in W2 is shown in Figure 9. Both maps show that the column position dominates the error term, with maximal flux
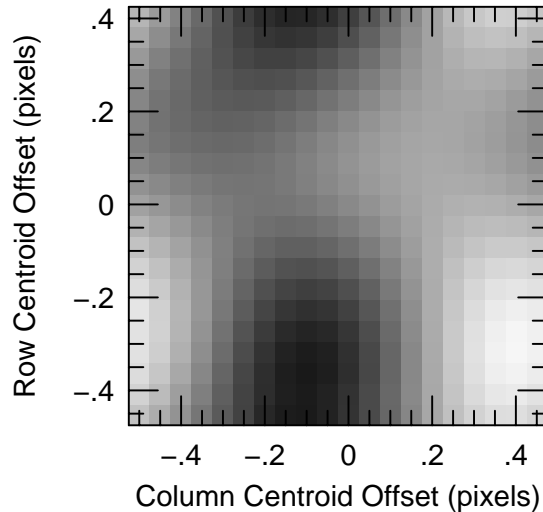

Fig. 9.— The photometric error map for a star also in the WFPC2 CCD W2 F555W data set, but separated from the star shown in Figure 1 by 147 pixels. The stretch is the same as in Figure 5.

detected for centroids falling between columns, and have about same dynamic range. The detailed structure of the first map is different enough from the second map, however, such that it would provide little help for correcting the photometry of a star imaged at the second location on W2.

The situation is somewhat better in the NIC3 camera, where the pixel response appears to dominate. Figure 10 shows the map for another star in the same H-band data set as the star shown in Figure 4. The peak-to-peak amplitude of the map is within a few hundredths of a magnitude of the map shown in Figure 8, and its morphology is similar enough so that corrections derived from the former star would work well for the latter.
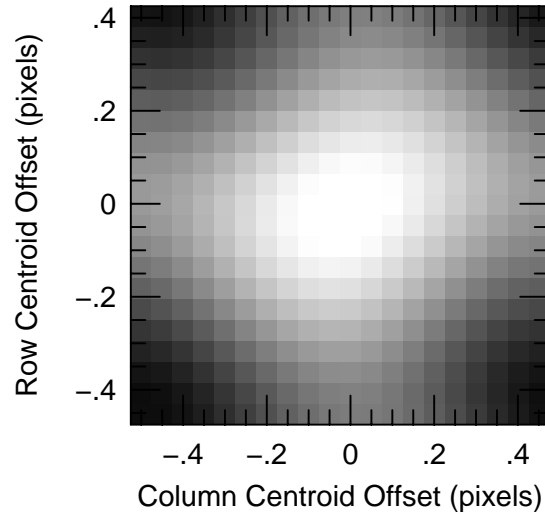
Fig. 10.— The photometric error map for a second star present in the NIC3 F160W data set, but displaced by about half of the field from the star shown in Figure 4. The stretch is the same as in Figure 8.

Regardless of the utility of the present error maps for correcting undersampled stellar photometry directly, they do show what errors are likely to be encountered, and how well various dither patterns sample the error pattern. The present analysis emphasizes constructing a well-sampled image from a dither set to counter undersampling present in any single image. Clearly, a simpler approach of averaging the photometry from a star observed at different positions in general may reduce the photometric scatter due to undersampling by $\sqrt{N}$, where N is the number of dither steps available. A caveat is that neither the error maps, nor dither pattern are necessarily random, thus this simple scheme may produce less noise reduction than expected or still include biases among stars at differing positions, particularly if the number of dithers is small. The large range of the NIC3 error maps further imply that an extremely large data set may be required to obtain 1% photometry by the simple combination of random dithers.

In this context, I've been surprised by how often dithered image sets fail to sample the full range of fractional pixel space adequately. Figure 11, for example, shows the fractional dithers realized in the NIC3 HDFS image set. Despite the availability of nearly 100 images, the pattern misses covering the fractional pixel space as well as a simple regular 3×3 pattern would; note that no or very few dithers fall within three of the corners of the figure. To be fair, the dithers in the HDFS program were optimized for the other cameras on board *HST*, rather than NIC3, but clearly the assumption that such a large data set would randomly sample the full fractional space is not justified. In the present case, failure to include many dithers landing near the pixel corners in the case of NIC3 clearly produces a strong bias, since these are the regions in which the flux
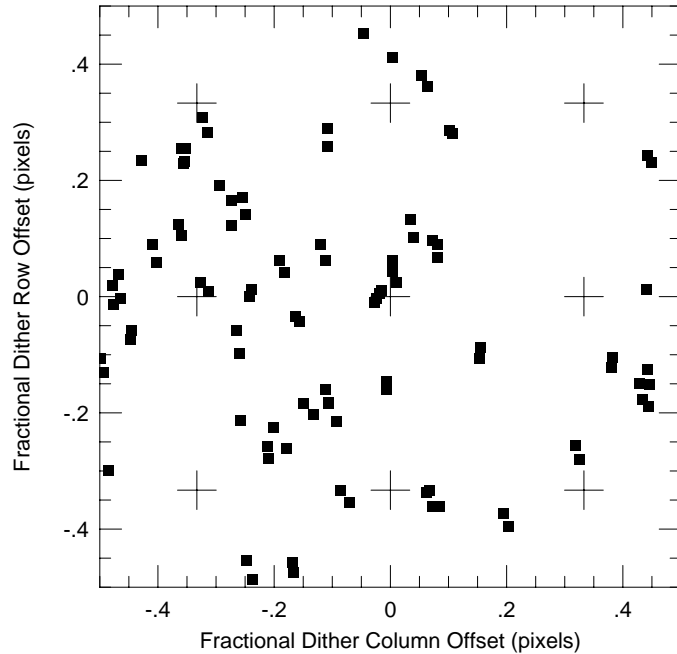
Fig. 11.— The fractional pixel locations of the dithers for the F160W NIC3 data set are shown. Crosses mark a putative 3×3 dither pattern.

deficit due to undersampling is most severe; further, other stars in the same image set will have their dithers phased differently, thus biases due to incomplete dither coverage in this particular image set would be presented as large scatter among stars at different locations. Lastly, I note that these biases will not be removed by image reconstruction algorithms, such as *Drizzle,* that simply redistribute the image flux; in the end one is effectively still just averaging the stellar images. The Fourier reconstruction methods that I discuss in Lauer (1999), in contrast, can reconstruct an unbiased PSF from even non-optimal dither patterns, such as that in Figure 11. The trick is that the complete set of Fourier components that describe the PSF may still be represented in the dither set and isolated algebraically, even if it is not optimally encoded in the data.

2.3. Computing the Centroid of an Undersampled PSF

While the error maps encode the photometric error as a function of the fractional location of the PSF centroid, an important caveat is that measurement of the centroid itself will be affected by undersampling. This issue is central to the concerns of Anderson & King (1999), who discuss methods to obtain high precision relative astrometry on WFPC2 images for the goal of measuring the relative proper motions of stars within globular clusters. I will thus not dwell extensively on this issue, myself. Nevertheless, being able to obtain accurate centroids of PSFs is critical to

constructing the effective PSF in the first place, and then evaluating the photometric error of stars at any position in the image set.

Figure 12 gives an error map of the total differences between the centroids of undersampled
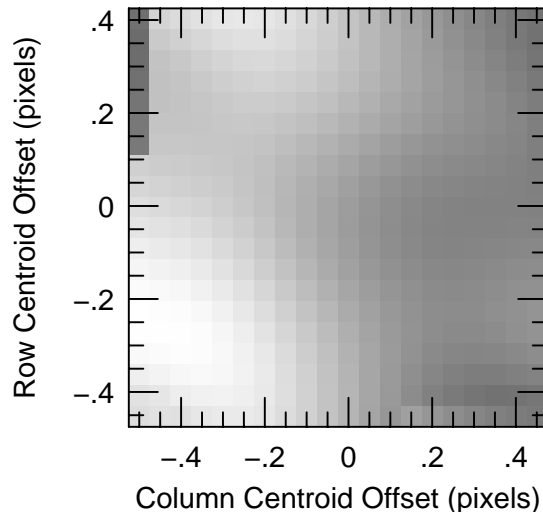
Fig. 12.— An error map showing the total radial difference between centroids measured from extracted undersampled NIC3 H-band PSFs as a function of the true fractional displacement of the effective PSF (shown in Figure 4) from a pixel center. White corresponds to the maximal error seen of 0.27 pixels.

NIC3 H-band PSFs (drawn from the effective PSF presented in Figure 4) as a function of the true offset. In this case, the centroids were computed as the simple center of weight of a 5×5 box centered on the brightest pixel of the extracted PSF. The size of the error varied smoothly over the fractional shift domain, ranging from 0.12 to 0.27 pixels; if the computed centroids were used to look up the corresponding H-band photometric error in Figure 8, clearly the implied photometric correction could be substantially in error. Now it is true that this simple method of calculating centroids perhaps would never be the algorithm of choice for undersampled data, but this is the point — methods that do work well for centroiding well sampled PSFs may work poorly for undersampled data, motivating the use of more sophisticated approaches.

The method that I have used to centroid undersampled PSFs is to cross-correlate them with a well-sampled PSF. This, of course, is fine if one has already generated a PSF from other stars in the image set, or can fold in knowledge of the pixel response with the construction of a theoretical PSF (see the next section). In practice, however, I've found that the Fourier reconstruction method is fairly tolerant of centroid errors, and for WFPC2 and NIC3 data, an initial *ad hoc* effective PSF can be constructed from simple centroiding algorithms as discussed in the previous paragraph. The penalty is some blurring in the PSF core, but the *ad hoc* effective PSF can

then be used to derive more accurate centroids from the cross-correlation method — indeed, this can lead to an iterative loop where one is continually refining the centroids and the effective PSF in successive stages. If a pre-existing effective PSF is available, however, a critical step is to normalize it as closely as possible to the expected flux of the new PSF being constructed. With undersampled PSFs, particularly when much of the flux in contained in a single bright pixel, positional information is lost and there can be strong covariance between intensity scaling and centroid measurement, a point emphasized by Anderson & King (1999). Again in practice, however, I've found with WFPC2 and NIC3 data that one can readily construct an initial *ad hoc* PSF with a rough initial normalization. Lastly, of course, good information on the dither steps may already be available from external information, or measurements conducted from an ensemble of other sources in the image set.

2.4.   Isolating the Intra-Pixel Response Function

Equation (4) shows that the effective PSF, P', is the convolution of the intrinsic optical PSF with the pixel response, $\mathcal{R}$. For the discussion so far, there has been no need to separate the two terms contributing to P'; however, if knowledge of the optics-only PSF is available, or it can be calculated by an algorithm such as Tiny Tim (Krist & Hook 1997), then it may be possible to isolate the pixel response by deconvolution. If $\mathcal{R}$ is largely constant over the array, as Jorden, Deltron, & Oates (1994) suggest is true for CCDs, then is may be possible to use it in conjunction with theoretical spatially-variable PSFs to construct improved subsampled PSFs at any point within the field.

Figure 13 shows an attempt to isolate $\mathcal{R}$ for the F555W filter and the W2 CCD of WFPC2 by
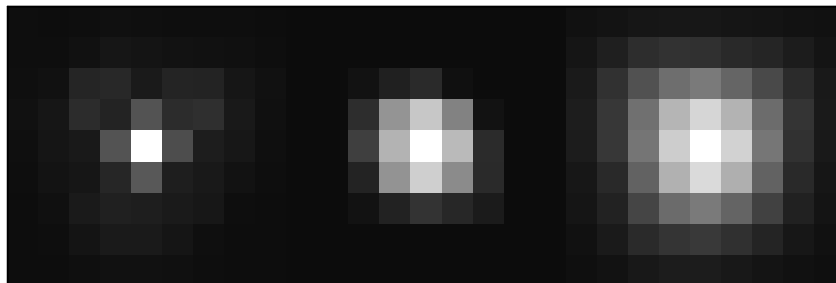

Fig. 13.— The F555W subpixel response for the W2 CCD in shown in the center with 3×3 subsampling. The total area of each image is 9×9 subpixels, or 3×3 full WFC pixels. The core of the subsampled reconstructed PSF (the same star as in Figure 1) is at right, and the Tiny Tim PSF estimate is at the left. The stretch is linear, and all three images are normalized to the same peak intensity.

deconvolving the effective PSF in Figure 1 with a theoretical PSF constructed with the Tiny Tim package. The particular star selected has $V - I = 1.09$ (in the WFPC2 filters), which corresponds very closely to spectral type K0. The theoretical PSF was constructed for the star's location on W2 and with 3×3 subsampling. Deconvolution was done with 160 iterations of Lucy-Richardson deconvolution (Richardson 1972; Lucy 1974); however, convergence occurred well in advance of this many iterations.

The F555W $\mathcal{R}$ kernel is in excellent agreement with previous, but full-pixel rather than sub-pixel estimates of the WFPC2 pixel response. Holtzman et al. (1995) noted that some diffusion of light across pixel boundaries appeared to be occurring in the WFPC2 CCDs. Krist & Hook (1997) suggest a kernel that has 75% of its integral in a central pixel, with 5% flanking pixels in the row and column of the central pixel. The present kernel is given below with 3×3 subsampling, with the pixel values given as percentages of the total integral.

$$
\begin{array}{ccccc}
0.3 & 1.1 & 1.7 & 0.2 & 0.0 \\
1.8 & 7.4 & 10.2 & 6.4 & 0.4 \\
2.8 & 9.1 & 13.2 & 9.5 & 1.7 \\
1.3 & 7.4 & 10.6 & 7.0 & 1.7 \\
0.4 & 1.2 & 2.2 & 1.5 & 0.8
\end{array}
\tag{7}
$$

Pixels outside the 5×5 kernel listed are essentially zero; the diffusion out of the central (full-sized) pixel is actually limited to only a thin margin a single subpixel in width.

Figure 14 shows a similar attempt to isolate $\mathcal{R}$ for the F110W filter in the NIC3 camera. As
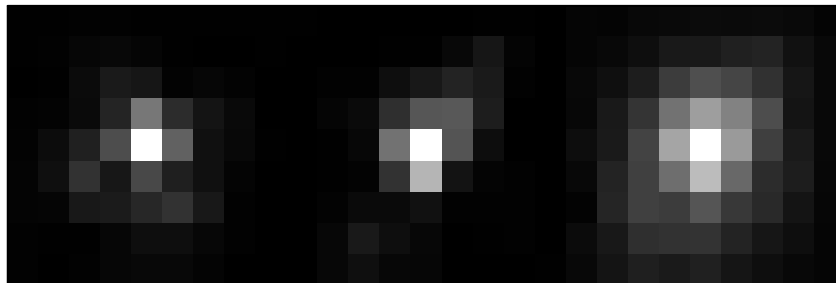

Fig. 14.— The F110W subpixel response for NIC3 in shown in the center with 3×3 subsampling. The total area of each image is 9×9 subpixels, or 3×3 full NIC3 pixels. The core of the subsampled reconstructed PSF (the same star as in Figure 3) is at right, and the Tiny Tim PSF estimate is at the left. The stretch is linear, and all three images are normalized to the same peak intensity.

expected given the more severe undersampling effects in NIC3, the $\mathcal{R}$ kernel is more compact and sharply peaked than the WF2 pixel response. The NIC3 pixel kernel is given below with 3×3

subsampling, with the pixel values given as percentages of the total integral.

$$\begin{array}{ccccc}
0.2 & 1.2 & 2.2 & 3.1 & 2.3 \\
0.9 & 4.2 & 7.5 & 7.7 & 2.5 \\
0.6 & 10.0 & 22.3 & 7.4 & 1.2 \\
0.3 & 4.4 & 15.9 & 1.7 & 0.4 \\
0.8 & 0.9 & 1.5 & 2.5 & 0.2
\end{array} \tag{8}$$

3. Discussion and Summary

3.1. Photometry and the Structure of a Pixel

A one-sentence summary of this paper is that the precision of stellar photometry may be significantly limited when the PSF is undersampled. The common assumption that a CCD consists of an array of contiguous and uniform pixels is an excellent initial approximation, but is not correct in detail. One may be tempted to adopt a refined picture in which the array consists of uniform pixels, but surrounded by dead "moats;" however, this still is likely to be an oversimplification. In truth, the sensitivity pattern within a pixel is likely to be complex and highly dependent on the specifics of the detector architecture — indeed, once one allows for possible diffusion of photons or photoelectrons within the detector, the total spatial response function of a single pixel may be more complex than can be described by pure sensitivity variations alone. The import of the pixel response depends directly on the severity of the undersampling and the structural content of the astronomical source being imaged. It should also be understood that the pixel response may be even more important than the core of the optics PSF in setting the final resolution of an image.

3.2. Dithering Strategies

If countering the effects of undersampling on stellar photometry is important, then I argue that the best solution is to dither the images in a regular pattern that permits easy reconstruction of a well-sampled superimage. The information content of the superimage is as complete as can be allowed for the particular properties of the camera's detector and optics.

The optimal dither pattern is a regular $N \times N$ grid of $1/N$ subpixel steps. In practice one may want to add full integral steps to the fractional steps as a way of stepping over hot pixels, bad columns, traps, or any other compact detector defects; however, if there are significant scale variations over the detectors field, then it is best to keep the total spatial extent of the dither pattern as compact as possible. In an ideal case, one would also obtain two or more exposures at each dither step, so as to eliminate cosmic rays events, or any other variable noise feature. If large angular steps are desirable as well to counter any large scale variations in the detector response, then I suggest that the best way to proceed is to obtain the full data set as in subsets of complete

compact dither sequences separated by the larger offsets. Each subset will make a well-sampled superimage; combining the superimages into a final image is then simple.

If a regular dither pattern can be executed exactly, then construction of a superimage requires nothing fancier than simple interlacing of the individual images. If the dither positions fall somewhat away from their optimal locations, but the fractional pixel domain still has good coverage, or the image set is over-determined, then I suggest the Fourier method used in this paper as a possible reconstruction algorithm. However, even if no formal reconstruction is attempted, a regular dither pattern will optimize the information content of the image set. Lastly, I emphasize that in general this is a fully two-dimensional problem. While the WFCP2 pixel response, for example, is more important in the column direction, it cannot be cleanly separated into separate x and y functions. For cameras like NIC3, two orthogonal one-dimensional patterns will fall well short of mapping the fractional pixel domain.

3.3. Designing Undersampled Cameras

The choice of a pixel scale for an astronomical camera often requires a compromise between having a large a field as possible versus obtaining well sampled images. Since even rather poorly sampled CCD cameras, such as the WFC channel of WFPC-2, produce excellent stellar photometry for most problems, it is difficult to argue against tipping their design towards the largest field that the optics can accommodate. However, for many of the near and mid-IR cameras contemplated for space missions now in the early design phases, one must recognize that IR-arrays may be less forgiving of undersampled PSFs and may limit the photometric accuracy to unacceptable levels if the undersampling is too extreme.

If designing a Nyquist-sampled camera causes unacceptable limitations on the field, however, then I suggest that one may want to include a dither capability directly in the camera, itself. *HST* has demonstrated the value of dithering undersampled images, but dithering *HST* images is both awkward and prone to error or non-optimal patterns since the full spacecraft must be moved. An in-camera dither capability, in contrast, can likely be made to be simple, highly accurate, and easy to invoke; ideally, the dither capability would be accurate enough to allow for direct interlace reconstruction of the superimage. The caveats are that the dithering must be conducted on timescales shorter than those on which significant variation in image structure will occur; when readout noise or overhead becomes significant the minimum timescale between dithers may make dithering difficult. Lastly, I emphasize that even fine dithering is unlikely to lift the effects of severe undersampling. As a camera becomes increasingly poorly sampled, not only does the size of the image set required rise as the square of the inverse dither step (and with it the attendant difficulty of maintaining a stable image over the length of a dither sequence), but the precision to which small errors in the pattern can be detected and corrected for declines, making accurate image reconstruction all the more difficult. In practice, pushing beyond $N = 3$ subsampling for either WFPC-2 or NIC3 appears to be highly cumbersome, and thus may imply final upper limits

to the pixel scales of other cameras in general if accurate photometry is both important and limited by undersampling.

REFERENCES

Anderson, J. & King, I. R. (1999), in preparation

Bracewell, R. N. (1978), The Fourier Transform and its Applications, p. 201-202 (McGraw-Hill)

Fruchter, A. S. & Hook, R. N. 1999 PASP, submitted; astro-ph/9808087

Holtzman, J., et al. 1995, PASP, 107, 156

Jorden, P. R., Deltron, J. -M., & Oates, A. P. 1994, Proceedings of Instrumentation in Astronomy VIII, SPIE, 2198, 836

Krist, J. & Hook, R. 1997, *The Tiny Tim User's Guide* (version 4.4) (Baltimore:STScI)

Lauer, T. R. 1999 PASP, 111, 227

Lucy, L. B. 1974, AJ, 79, 745

Mighell, K. J. 1997, AJ, 114, 1458

Richardson, W. H. 1972, J. Opt. Soc. A., 62, 52

Schechter, P. L., Mateo, M., Saha, A. 1993, PASP, 105, 1342

Stetson, P. B. 1994, PASP, 106, 250